Contents lists available at ScienceDirect

Applied Surface Science

journal homepage: www.elsevier.com/locate/apsusc

Full Length Article

In_2O_3/boron doped g-C_3N_4 heterojunction catalysts with remarkably enhanced visible-light photocatalytic efficiencies

Xiaoyan Jin[a,1], Qingmei Guan[a,1], Tong Tian[a], Huiquan Li[a], Yan Han[a], Fuying Hao[a], Yumin Cui[a], Wenyong Li[b], Yongfa Zhu[a,c], Yan Zhang[a]

[a] Anhui Provincical Key Laboratory for Degradation and Monitoring of Pollution of the Environment, School of Chemistry and Materials Engineering, Fuyang Normal University, Fuyang 236037, PR China

[b] Anhui Province Key Laboratory of Environmental Hormone and Reproduction, Biology and Food Engineering School, Fuyang Normal University, Fuyang 236037, PR China

[c] Collaborative Innovation Center for Regional Environmental Quality, Tsinghua University, Beijing 100084, PR China

ARTICLE INFO

Keywords:
In_2O_3/g-C_3N_4B heterojunction
Degradation of TH
NO conversion
CH_4 generation

ABSTRACT

Novel In_2O_3/boron doped graphite-like carbon nitride (In_2O_3/g-C_3N_4B) heterojunction catalysts were successfully fabricated via a facile water-bath combined with calcination method. The resulting 5% In_2O_3/g-C_3N_4B catalyst with a proper In_2O_3 and B content exhibits excellent visible-light photocatalytic activities. Its conversion ratio for tetracycline hydrochloride (TH) and nitric oxide (NO) is 2.0, 1.9 times higher than that of In_2O_3, g-C_3N_4, g-C_3N_4B, g-C_3N_4B-R (reference sample), respectively. And its CH_4 evolution rate is 9.0, 3.6, 2.2, 2.5 times higher than that of In_2O_3, g-C_3N_4, g-C_3N_4B, g-C_3N_4B-R, respectively. The remarkably enhanced photocatalytic properties are mainly attributed to the result that an appropriate boron and In_2O_3 modified the g-C_3N_4 promoted the efficient separation and transfer of photoinduced electrons and holes from the heterojunction interface by the band alignment between In_2O_3 and g-C_3N_4B. The probable mechanism on the activity enhancement was also discussed. Moreover, 5% In_2O_3/g-C_3N_4B shows good activity stability as evidenced by three recycling reactions. This work offers some useful insights to design and fabricate other highly efficient and stable g-C_3N_4-based heterojunction multifunctional materials for energy conversion and environmental restoration applications in the near future.

1. Introduction

Two dimensional (2D) graphitic carbon nitride (g-C_3N_4) photocatalytic material, as a promising organic semiconductor for H_2 production, pollutants treatment and CO_2 reduction, has caused remarkable attention recently because of its unique optical and electronic properties that are very important in photocatalysis, non-toxicity and convenient synthetic routes [1–8]. However, for the g-C_3N_4 with a band gap (E_g) of ~2.7 eV, the poor photocatalytic efficiency induced by the quick recombination of photo-induced electrons and holes limits its practical applications [9–17].

To perfect the photocatalytic material, a great quantity of studies

heterojunction by heating $In(Ac)_3$ and g-C_3N_4 in autoclave and demonstrated effective charge separation on the heterointerface. Recently, a kind of ternary composite photocatalyst by coupling two metal oxides semiconductor (TiO_2 and In_2O_3) with g-C_3N_4 was synthesized and high visible-light photocatalytic activity was exhibited [39].

Naturally, a novel design is proposed that boron doping and the introduction of In_2O_3 to g-C_3N_4 occur simultaneously. Whether the synergistic effect is more excellent? Motivated by the above concerns, in the present work the heterostructured In_2O_3/g-C_3N_4B catalysts were prepared through a facile water-bath calcination method, and the information of morphology, structure and optical property of In_2O_3/g-C_3N_4B catalysts was studied. The activities of In_2O_3/g-C_3N_4B catalysts were researched by tetracycline hydrochloride (TH) degradation and nitric oxide (NO) conversion, and carbon dioxide (CO_2) reduction. Based on experimental outcomes, the probable mechanism of activity improvement for the In_2O_3/g-C_3N_4B catalysts was discussed.

2. Experiments

2.1. Catalysts synthesis

In_2O_3/g-C_3N_4B catalysts were fabricated via a simple water-bath combined with calcination method. Boron doped g-C_3N_4 (g-C_3N_4B) was prepared as follows: 2.0, 4.0, 10, or 20 mg sodium tetraphenylboron ($C_{24}H_{20}BNa$) and 10 g urea were dissolved into distilled water (10 mL), followed by stirring under 353 K for 5.0 h, and then the product was calcined under 823 K for 2.0 h. After cooled naturally, yellow product was grounded to obtain a powder sample. The synthesized B-doped g-C_3N_4 catalysts are denoted as g-C_3N_4B-x, and x is the mass (mg) of $C_{24}H_{20}BNa$ introduced into the precursor solution. For comparative study, a boron doped g-C_3N_4 reference sample (g-C_3N_4B-R) with the highest activity in the literature (Angewandte Chemie International Edition, 2013, 52, 1735–1738) [40] was also synthesized. To prepare the In_2O_3/g-C_3N_4B composites, 0.01 g, 0.05 g, 0.10 g and 0.20 g of In_2O_3 nanocrystals (commodity) and 1.0 g of the as-synthesized g-C_3N_4B-4 were added into 10 mL absolute methanol, respectively. The resultant mixtures were ultrasonically treated for 5 min and then dried under 60 °C water-bath temperature. After being calcined at 723 K for 3 h, a series of In_2O_3/g-C_3N_4B catalysts with different weight concentration of In_2O_3, were denoted as 1%, 5%, 10% and 20% In_2O_3/g-C_3N_4B, respectively. The Pt loading on catalysts was prepared by a photo-deposition method [41].

2.2. Catalysts characterization

The crystalline phases of catalysts were analyzed by using a Bruker D8 X-ray diffractometer. The specific surface area of catalysts were measured by an ASAP2020 HD88 instrument at 77 K. Transmission electron microscopy (TEM) and higher-magnification transmission electron microscopy (HRTEM) images of catalysts were collected by a JEOL JEM2100F microscope. The X-ray photoelectron spectroscopy of catalysts was measured by a Thermo Scientific K-Alpha spectrometer. At 400 nm excitation wavelength, the photoluminescence spectroscopy was obtained by a CARY Eclipse fluorescence spectrophotometer. The electron paramagnetic resonance spectra were recorded by a Bruker model A300 spectrometer. Using $BaSO_4$ as the reference, the UV–Vis diffuse reflection spectroscopy (DRS) was done at a Varian Cary 500 Scan. Electrochemical measurements of g-C_3N_4, g-C_3N_4B and 5% In_2O_3/g-C_3N_4B samples were also carried out by following the steps of this reference [42].

2.3. Activity evaluation

Activity evaluation experiments were carried out under visible-light ($\lambda > 420$ nm) irradiation, by adding 200 mg photocatalysts into 40 mL of 5.0 mg/L tetracycline hydrochloride (TH) solution. In order to establish an adsorption–desorption equilibrium, the solution was magnetically stirred for 0.5 h in the dark. After different irradiation time, the concentration of TH solution was measured by using a spectrophotometer (TU-1901). The change of total organic carbon (TOC) of 5% In_2O_3/g-C_3N_4B reaction process was measured by using a TOC analysis system (Shimadzu TOC-L CSH).

NO conversion was studied by a flow reactor system under visible-light ($\lambda > 420$ nm) irradiation for 4 h. The photocatalyst (0.1 g) was uniformly coated onto a dish with a diameter of 8.0 cm, and then it was dried at 80 °C. Initial NO concentration is 400 ppb, and its flow rate is 3 L/min. After attaining the equilibrium of adsorption–desorption, the Xe arc lamp was turned on, and the concentration of NO was continually measured by a chemiluminescence NO analyzer.

The photocatalytic reduction of carbon dioxide (CO_2) into methane (CH_4) reaction was performed as follows. Typically, the disperse photocatalyst (50 mg) of small glass cell bottom was located in a Pyrex glass cell bottom, connected with a closed system. The reaction system volume was ~230 mL. After vacuum-treating the reaction setup for three times, the high purity CO_2 gas entered into the reaction setup to attain an ambient pressure, and the system air was replaced by CO_2. And then, the reactor was injected into 2.0 mL H_2O by a liquid syringe. Next, the reactor was placed in darkness for 2.0 h to reach an adsorption-desorption equilibrium. Finally, the reactor was irradiated under $\lambda > 420$ nm. Within a given time interval, the reaction cell was continually extracted gaseous product (0.5 mL) to check CH_4 concentration by a Shimadzu gas chromatograph (GC-2014, Ar carrier) during irradiation.

3. Result and discussion

3.1. Composition, morphology, and structure of catalysts

The crystalline phases of pure g-C_3N_4, g-C_3N_4B, 1% In_2O_3/g-C_3N_4B, 5% In_2O_3/g-C_3N_4B, 10% In_2O_3/g-C_3N_4B, 20% In_2O_3/g-C_3N_4B and pure In_2O_3 samples were shown in Fig. 1. All the patterns except pure In_2O_3 show characteristic diffraction peak of g-C_3N_4 at about $2\theta = 27.4°$, which is ascribed to (0 0 2) reflection of the interlayer stacking peak of conjugated aromatic systems [43]. Meanwhile, from the XRD patterns in Fig. 2, it can be noticed that g-C_3N_4 diffraction peak (0 0 2) intensity decreased with the increasing B content, but the B-doping process did not change its crystal structure. It can be also observed from Fig. 1 that the diffraction peaks at 21.5°, 30.5°, 35.6°, 51.0° are perfectly indexed to the (2 1 1), (2 2 2), (4 0 0), (4 4 0) crystal planes in the cubic In_2O_3 (JCPDS No. 00-006-0416), respectively. Obviously, the diffraction peaks of In_2O_3 are strengthened gradually with increasing In_2O_3 amount at the expense of those of g-C_3N_4B, confirming that the co-

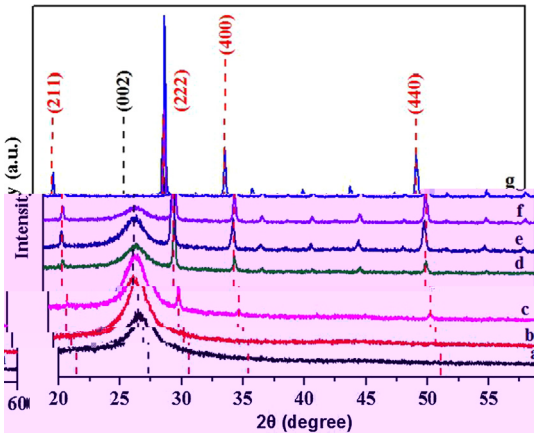

Fig. 1. XRD patterns of (a) g-C_3N_4, (b) g-C_3N_4B, (c) 1% In_2O_3/g-C_3N_4B, (d) 5% In_2O_3/g-C_3N_4B, (e) 10% In_2O_3/g-C_3N_4B, (f) 20% In_2O_3/g-C_3N_4B and (g) In_2O_3 samples.

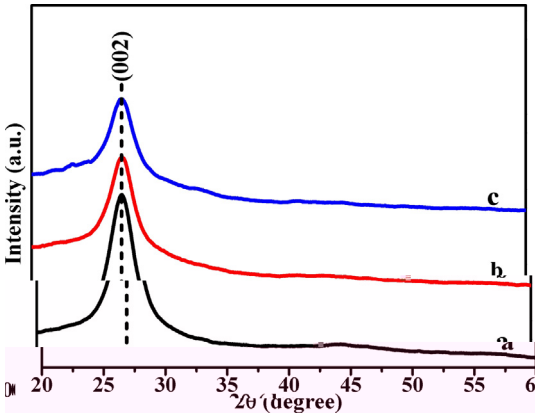

Fig. 2. XRD patterns of (a) g-C_3N_4B-2, (b) g-C_3N_4B-4, (c) g-C_3N_4B-10 samples.

existence of both In_2O_3 and g-C_3N_4B crystalline phases of In_2O_3/g-C_3N_4B samples. No other characteristic peaks are detected in the In_2O_3/g-C_3N_4B samples, suggesting that no impurity species were formed in addition to g-C_3N_4B and In_2O_3.

The results of specific surface area for g-C_3N_4, g-C_3N_4B, In_2O_3, and In_2O_3/g-C_3N_4B samples were displayed in Table 1, and it can be seen that the g-C_3N_4B (78–94 m^2/g) and In_2O_3/g-C_3N_4B samples (83–91 m^2/g) show a higher specific surface area than that of g-C_3N_4 (46 m^2/g) or In_2O_3 (37 m^2/g), which is beneficial for enhancing the photoactivity of g-C_3N_4B and In_2O_3/g-C_3N_4B samples.

The morphologies of g-C_3N_4, g-C_3N_4B, In_2O_3, In_2O_3/g-C_3N_4B samples were shown in Fig. 3. It can be noticed that the g-C_3N_4 sample shows a layered platelet-like shape [44] (Fig. 3A) and the g-C_3N_4B sample possesses a thin, silk-like hybrid nanostructure [40] (Fig. 3B). TEM images of pure In_2O_3 nanoparticles and In_2O_3/g-C_3N_4B hybrid samples were shown in Fig. 3C and Fig. 3D, respectively. It can be seen that many dark In_2O_3 nanoparticles tightly aggregates on the surface of g-C_3N_4B, corroborating that In_2O_3/g-C_3N_4B heteroarchitectures are successfully constructed. In addition, the HRTEM images (Fig. 4) of In_2O_3 and 5% In_2O_3/g-C_3N_4B samples revealed the existence of In_2O_3 nanocrystals, and the lattice fringes with d spacing of 0.294 nm could be assigned to the (2 2 2) crystal plane of cubic In_2O_3 [38].

These In_2O_3/g-C_3N_4B heterostructures were further also characterized by X-ray photoelectron spectroscopy. In the g-C_3N_4 and g-C_3N_4B samples, the C 1s XPS spectrum (Fig. 5A) could be deconvoluted into two peaks, the peak at 284.6 eV is attributed to carbon impurities, the peak at 287.9 eV is attributed to an sp^2-bonded carbon (C—C═N) [40,45]. The N 1s XPS spectrum (Fig. 5B) could be deconvoluted into three peaks at 398.4, 399.6, and 400.7 eV, which are ascribed to sp^2-bonded nitrogen in N-containing aromatic rings (C—N═C), the tertiary nitrogen N— $(C)_3$ groups and the amino groups (C—N—H), respectively

Table 1
The specific surface areas, pore sizes and pore volumes data of the as-prepared catalysts calculated by BET and BJH methods.

Sample	Specific surface area (m^2/g)	Pore size (nm)	Pore volume (cm^3/g)
g-C_3N_4	46	26.7	0.216
g-C_3N_4B-2	78	25.9	0.532
g-C_3N_4B-4	94	27.4	0.561
g-C_3N_4B-10	85	26.3	0.541
1% In_2O_3/g-C_3N_4B-10	91	26.6	0.552
5% In_2O_3/g-C_3N_4B-10	89	27.6	0.548
10% In_2O_3/g-C_3N_4B-10	87	26.5	0.545
20% In_2O_3/g-C_3N_4B-10	83	26.1	0.538
In_2O_3	37	3.8	0.091

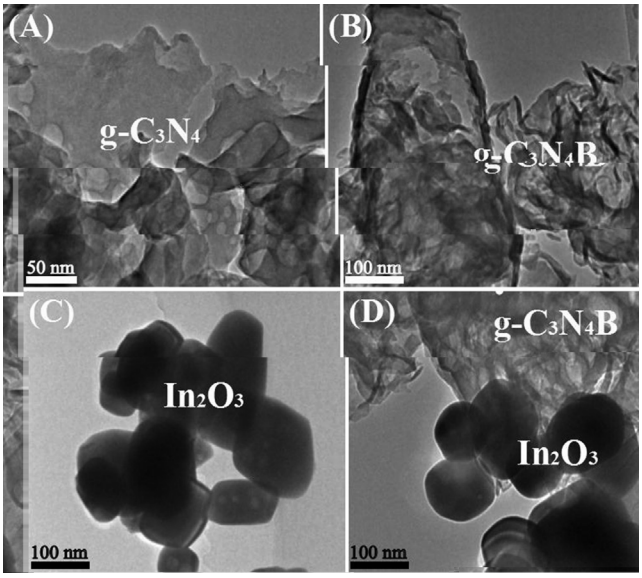

Fig. 3. TEM images of (A) g-C_3N_4, (B) g-C_3N_4B, (C) In_2O_3 and (D) 5% In_2O_3/g-C_3N_4B.

[40,45]. However, In the 5% In_2O_3/g-C_3N_4B sample, the C 1s peak binding energy (288.1 eV) and the N 1s peaks binding energy (398.7, 400.2, and 401.0 eV) are respectively higher than that of the g-C_3N_4 or g-C_3N_4B sample, which are mainly attributed to the intense interaction between In_2O_3 and g-C_3N_4B or the heterojunction formation in the In_2O_3/g-C_3N_4B sample, showing a consistence with the result of the above XRD and TEM analyses. As can be observed from Fig. 6A, an obvious B 1s XPS peak with a binding energy of ~191.6 eV is seen for g-C_3N_4B and 5% In_2O_3/g-C_3N_4B samples, corresponding to the coordination of N-B-N [40]. In Fig. 6B, the In $3d_{5/2}$ and $3d_{3/2}$ signals of In_2O_3 and 5% In_2O_3/g-C_3N_4B samples are at 444.4 eV and 451.9 eV originating from In^{3+} [38,46].

The optical performance of g-C_3N_4, g-C_3N_4B, In_2O_3, In_2O_3/g-C_3N_4B samples was shown in Fig. 7A. Comparing with g-C_3N_4, the photo-absorption ability of g-C_3N_4B is stronger and the absorption edge extends towards visible-light region, as is also reported previously by Yan et al [32]. The light absorption threshold of pure In_2O_3 is 450 nm, corresponding to ~2.8 eV band gap (Fig. 7C), which is consistent with the band gap of the In_2O_3 reported in literature [46]. Compared to g-C_3N_4 and g-C_3N_4B, the absorption band edges of In_2O_3/g-C_3N_4B photocatalysts are obviously blue-shifted with the increase of In_2O_3 content (Fig. 7A), leading to an increase in band gap energy (Fig. 7B). Moreover, the light absorption range of In_2O_3/g-C_3N_4B is between the single phases of In_2O_3 and g-C_3N_4B, indicating a strong interaction between In_2O_3 and g-C_3N_4B produced a synergistic effect in the In_2O_3/g-C_3N_4B photocatalyst [4], which is favorable to promote the separation and migration of the photogenerated charges, thus improving photocatalytic activity.

3.2. Activity and stability

The activities of g-C_3N_4, In_2O_3, g-C_3N_4B and In_2O_3/g-C_3N_4B catalysts with different In_2O_3 weight percentage were evaluated by the degradation test of tetracycline hydrochloride (TH) (Fig. 8A). From Fig. 8A, one can see that there is almost no change of TH concentration under $\lambda > 420$ nm light irradiation for 3.0 h in a lack of catalyst, showing that TH self-photodegradation can be ignored. Compared with g-C_3N_4, all the three B-doped g-C_3N_4 catalysts display better photocatalytic activity (Fig. 9). After 3 h irradiation, the TH degradation ratio of g-C_3N_4B-4 is 44.7%, which is 1.5 times that of g-C_3N_4. When In_2O_3 is used as the photocatalyst, only ~25% of TH is degraded after 3 h,

showing a poor photocatalytic property. Although g-C_3N_4B-4 exhibits the better photodegradation activity compared with the undoped g-C_3N_4, only less than ~45% of TH is degraded. In Fig. 8A, it can also be observed that the higher photodegradation performance of TH is observed in the presence of In_2O_3/g-C_3N_4B heterojunction catalysts re-

Obviously, the CH_4 evolution rate of 5% In_2O_3/g-C_3N_4B (physical mixture) is lower than that of the 5% In_2O_3/g-C_3N_4B heterojunction catalyst, showing the merit of hybridization.

The stability of 5% In_2O_3/g-C_3N_4B was also studied by recycling the catalyst for TH degradation, NO conversion, and CO_2 photocatalytic reduction into CH_4 under $\lambda > 420$ nm light irradiation. It can be clearly seen in Fig. 11 that there was no obvious deactivation on the activity after three consecutive runs, and the crystal structure of 5% In_2O_3/g-C_3N_4B remained no change after TH degradation, NO conversion and CH_4 evolution (Fig. 12), indicating the excellent stability of 5% In_2O_3/g-C_3N_4B catalyst.

3.3. Scavenger in TH degradation

To elucidate the photocatalytic mechanism of In_2O_3/g-C_3N_4B catalysts, the active species of HT photodegradation process were studied by trapping experiments. Three different quenchers, AO (ammonium oxalate), IPA (isopropanol), and BQ (benzopuinone) were employed as h^+ (hole), $^{\cdot}OH$ (hydroxyl radical) and $^{\cdot}O_2^-$ (superoxide radical) scavenger [42,47], respectively. In Fig. 13, a slight variation with the addition of IPA in the TH degradation efficiency is observed, indicating that hydroxyl radical is not crucial activity species in TH degradation process. However, TH degradation is suppressed by the AO and BQ addition, implying that hole and superoxide radical play an important

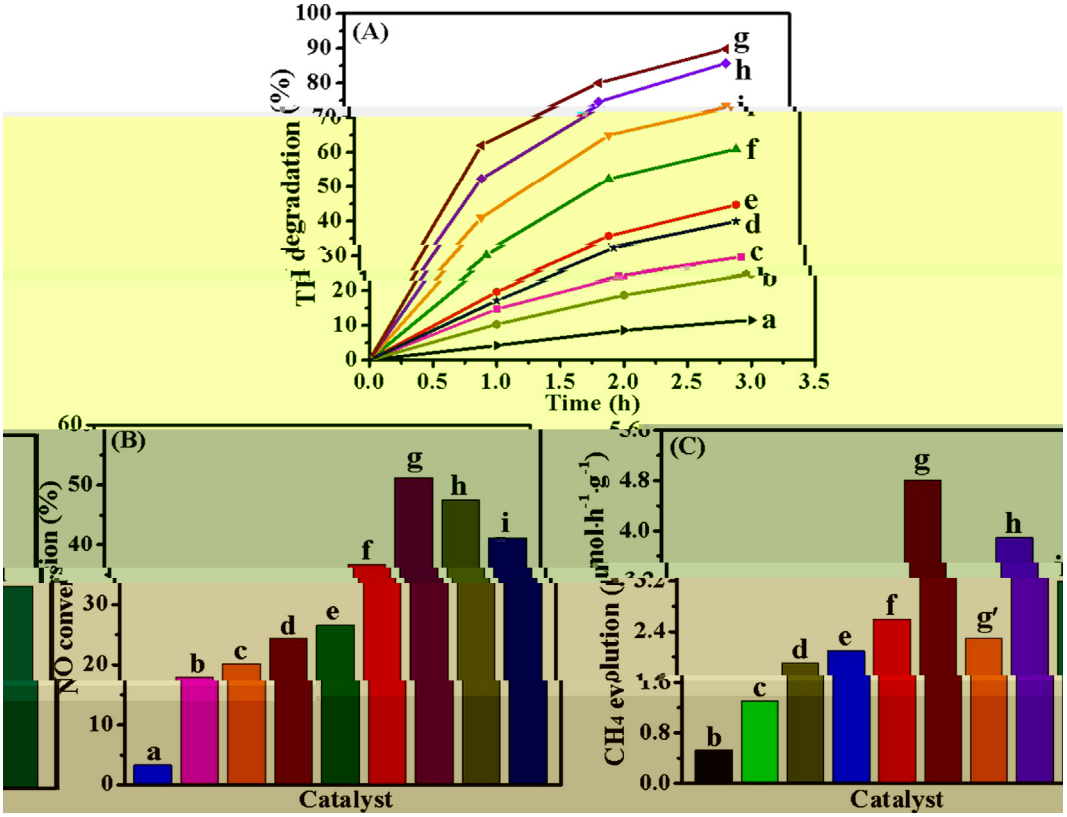

Fig. 8. Photocatalytic activity of TH degradation (A), NO conversion (B) and CH_4 evolution (C) for (a) blank, (b) In_2O_3, (c) g-C_3N_4, (d) g-C_3N_4B-R (reference sample), (e) g-C_3N_4B, (f) 1% In_2O_3/g-C_3N_4B, (g) 5% In_2O_3/g-C_3N_4B, (g') 5% In_2O_3/g-C_3N_4B (physical mixture), (h) 10% In_2O_3/g-C_3N_4B, (i) 20% In_2O_3/g-C_3N_4B catalysts.

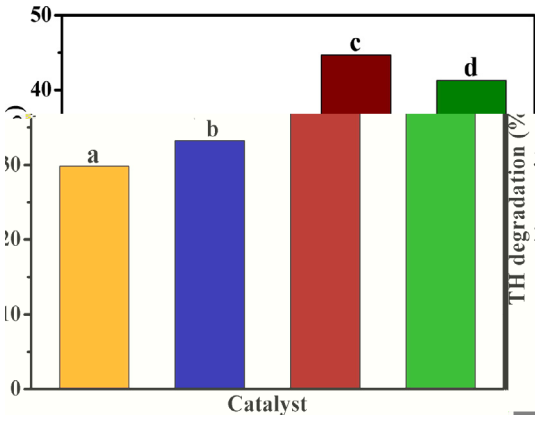

Fig. 9. The photocatalytic degradation of tetracycline hydrochloride (TH) for g-C_3N_4, (b) g-C_3N_4B-2, (c) g-C_3N_4B-4, and (d) g-C_3N_4B-10 catalysts under visible light irradiation (λ > 420 nm) for 3 h.

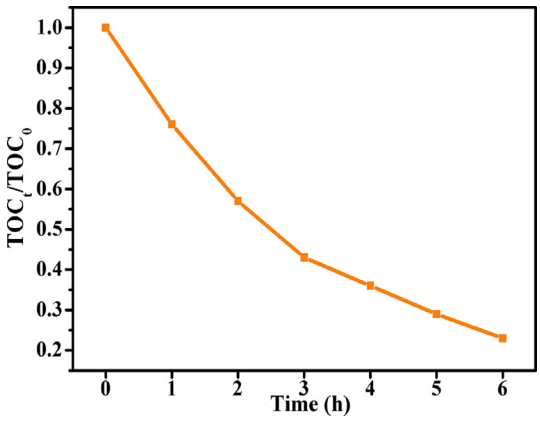

Fig. 10. Evolution of TOC during the course of photocatalytic degradation of tetracycline hydrochloride (TH) for 5% In_2O_3/g-C_3N_4B catalyst under visible light irradiation.

degradation ratio can also be observed in N_2 atmosphere, showing that oxygen (O_2) can mainly act as e^- (electron) traps to produce superoxide radical ($^{\cdot}O_2^-$).

Therefore, the reactions of TH photodegradation are proposed in Eqs. (1)–(4):

$$\text{Catalyst } (In_2O_3/g\text{-}C_3N_4B) + h\nu \rightarrow e^- + h^+ \quad (1)$$

$$e^- + O_2 \rightarrow {}^{\cdot}O_2^- \quad (2)$$

$$\text{tetracycline hydrochloride} + h^+ \rightarrow \text{products} \quad (3)$$

$$\text{tetracycline hydrochloride} + {}^{\cdot}O_2^- \rightarrow \text{products} \quad (4)$$

3.4. Photocatalytic activity enhancement mechanism of In_2O_3/g-C_3N_4B

In g-C_3N_4 framework, the boron (B) doping enhanced its light absorption and reduced its band gap, as shown in Fig. 7. Moreover, the surface boron sites can serve as Lewis acids [40], improving the separation efficiency of photo-induced electron-hole pairs, and promoting the surface reactivity. Hence, a proper B-doping resulted in an obvious activity enhancement of g-C_3N_4 (Fig. 8).

Based on the above results, the activity enhancement of In_2O_3/g-C_3N_4B catalysts may mainly originate from the synergism of nonmetal boron, cubic In_2O_3 and 2D g-C_3N_4, and the formation of heterojunctions between In_2O_3 and g-C_3N_4B.

Compared with 20% In_2O_3/g-C_3N_4B (83 m^2/g), the 5% In_2O_3/g-

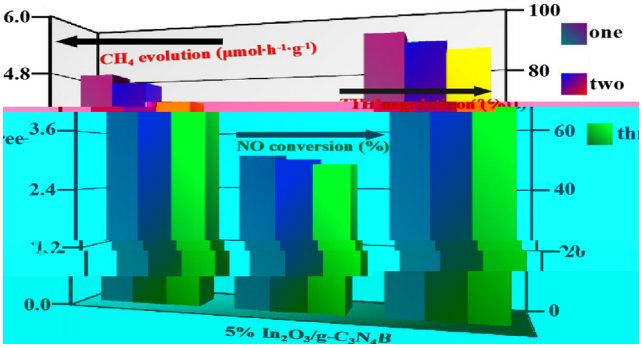

Fig. 11. Stability test of TH degradation, NO conversion and CH_4 evolution for 5% In_2O_3/g-C_3N_4B recycling three times under visible-light irradiation ($\lambda > 420$ nm).

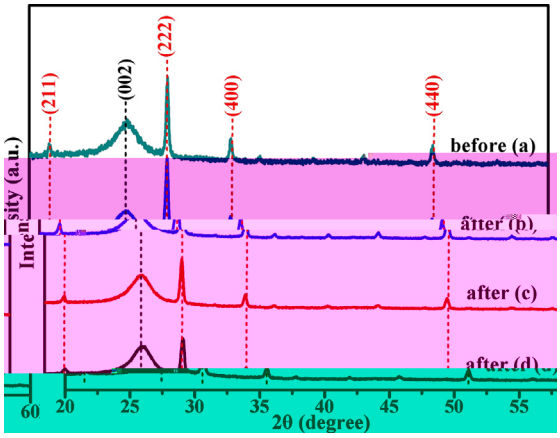

Fig. 12. XRD patterns of 5% In_2O_3/g-C_3N_4B before (a) and after TH degradation (b), NO conversion (c) and CH_4 evolution (d).

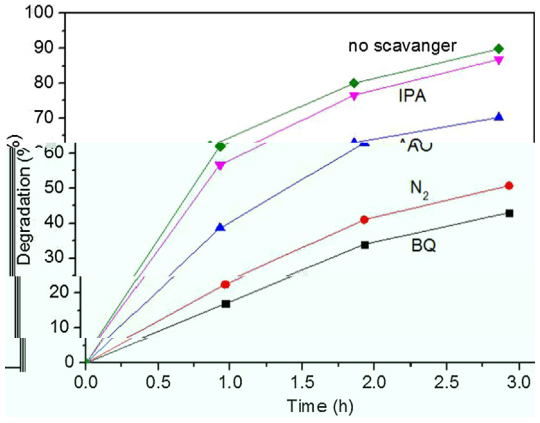

Fig. 13. The influence of various scavengers on the visible-light photocatalytic activity of 5% In_2O_3/g-C_3N_4B towards the degradation of TH.

C_3N_4B (89 m^2/g) catalyst has comparable specific surface areas and similar optical absorption (Fig. 7), but its photocatalytic activities in the photocatalytic conversion of TH and NO, and photocatalytic reduction of CO_2 (Fig. 8) three aspects are obviously higher than those of 20% In_2O_3/g-C_3N_4B, implying that there is another crucial factor influencing its photocatalytic property. Therefore, the separation efficiency of photo-generated carriers might play a crucial role in influencing the activity of catalysts. For the sake of revealing the charge separation on the interfaces of In_2O_3/g-C_3N_4B, the band potentials of g-C_3N_4B and In_2O_3 were investigated.

The photocatalytic performance is generally believed to be tightly

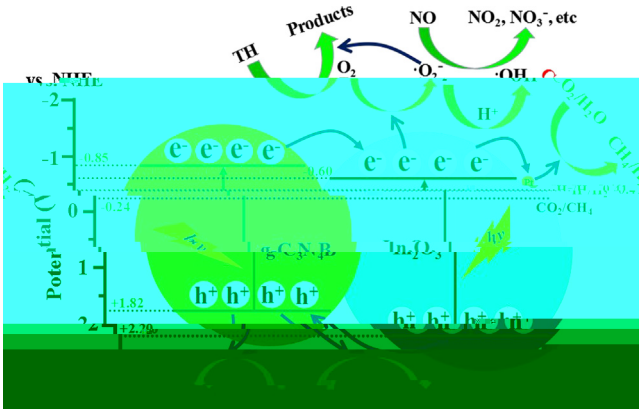

Fig. 14. The generation, transportation, and separation of visible-light-induced charge carries over the In_2O_3/g-C_3N_4B catalyst.

related to the redox potential and band structure of catalysts. Therefore, the activity enhancement mechanism for In_2O_3/g-C_3N_4B heterojunction catalyst may be reasonably explained by the scheme depicted in Fig. 14. According to theoretical calculation and previous reports [33,38,42,48,49], the top valence band potential (E_{VB}) and bottom conduction band potential (E_{CB}) for g-C_3N_4B and In_2O_3 are about +1.82 and −0.85 V, +2.20 and −0.60 V (vs. NHE), respectively. This indicates that the valence band top potential of In_2O_3 is more positive than that of g-C_3N_4B, whereas the conduction band bottom position of g-C_3N_4B is more negative than that of In_2O_3. When the In_2O_3/g-C_3N_4B photocatalyst is irradiated by visible light with the greater energy than the E_g (band-gap energy) of In_2O_3 and g-C_3N_4B, the e^- (electron) in the VB of In_2O_3 and g-C_3N_4B is excited to their CB, leading to the generation of hole in their VB. Then the band alignment between them can not only drive the photo-generated electrons in g-C_3N_4B to transfer towards the In_2O_3, but also drive the photo-induced holes in In_2O_3 transfer towards the g-C_3N_4B by valence band offset. Due to noble metal Pt can act as a superior acceptor and trapping site for photo-excited electrons, the photoinduced electrons would quickly transfer to the loaded Pt metal and then excited state electron can be quickly transfer to absorbed CO_2, forming the $^{\cdot}CO_2^-$ radical [50–52]. Meanwhile, the H^+ react with the excited electrons and form $^{\cdot}H$ radicals. Finally, $^{\cdot}CO_2^-$ and $^{\cdot}H$ radicals react with each other to produce CH_4 [51,52]. Thus the photo-generated electron-hole pairs will be separated effectively by an interface formed in the heterostructure, leading to the activity improvement eventually. Moreover, the phenomenon was also confirmed by below-mentioned photoluminescence spectroscopy (Fig. 15A), photocurrent tests and EIS (electrochemical impedance spectroscopy) results (Fig. 16). The photo-generated electrons gathered in the conduction band of In_2O_3 principally react with the surface hydroxyls and adsorbed oxygen (O_2) molecules, to ultimately form ·OH (hydroxyl radicals) and $\cdot O_2^-$ (superoxide radicals) reacting with the surface pollutants (TH, NO) of In_2O_3. At the same time, the corresponding photo-generated holes in the valence band of g-C_3N_4B can oxidize its surface pollutants (TH, NO) directly. And the possible reaction path is also shown in Fig. 14. Consequently, the heterojunction construction in the In_2O_3/g-C_3N_4B catalyst promoted the efficient separation of photo-generated electrons and holes, accelerating the photocatalytic reaction.

Photoluminescence (PL) emission spectroscopy is commonly performed to further verify the enhanced photo-excited charge separation efficiency [53]. The photoluminescence emission spectra of g-C_3N_4, g-C_3N_4B, 5% In_2O_3/g-C_3N_4B catalysts recorded under an excitation wavelength of 400 nm are presented in Fig. 15A. As can be observed, the peak positions of three catalysts are almost same, suggesting that there is no new photoluminescence with the introduction of boron and In_2O_3. The PL intensity of g-C_3N_4 is the highest among them, representing the high recombination probability of excited electrons and holes. Upon

doping boron into g-C_3N_4 the PL intensity obviouly decreased, which is in accordance with the reported result [32]. It should be noted that the 5% In_2O_3/g-C_3N_4B catalyst exhibits the lowest emission intensity, implying that the charge separation is greatly enhanced due to the co-operative effect of In_2O_3 and boron.

Fig. 15B shows the EPR (electron paramagnetic resonance) spectra of g-C_3N_4, g-C_3N_4B, 5% In_2O_3/g-C_3N_4B catalysts. A Lorentzian line was centered at *g*

(91643113), Natural Science Foundation of China (21807012), the Natural Science Foundation (1608085 MB34, gxgwfx2018059) and Major Projects for Provincial Discipline Construction ([2014]28) of Anhui Province in China, the project (XDHX2016002, XDHX201711, kytd201707, 201810371030) of Fuyang Normal University of China.

References

[1] Y. Zheng, L.H. Lin, B. Wang, X.C. Wang, Graphitic carbon nitride polymers toward sustainable photoredox catalysis, Angew. Chem. Int. Ed. 54 (2015) 12868–12884.
[2] W.-J. Ong, L.-L. Tan, Y.H. Ng, S.-T. Yong, S.-P. Chai, Graphitic carbon nitride ($g\text{-}C_3N_4$)-based photocatalysts for artificial photosynthesis and environmental remediation: Are we a step closer to achieving sustainability, Chem. Rev. 116 (2016) 7159–7329.
[3] Y.Y. Huang, D. Li, Z.Y. Fang, R.J. Chen, B.F. Luo, W.D. Shi, Controlling carbon self-doping site of $g\text{-}C_3N_4$ for highly enhanced visible-light-driven hydrogen evolution, Appl. Catal. B: Environ. 254 (2019) 128–134.
[4] H. Yang, B. Xu, S.S. Yuan, Q.T. Zhang, M. Zhang, T. Ohno, Synthesis of Y-doped CeO_2/PCN nanocomposited photocatalyst with promoted photoredox performance, Appl. Catal. B: Environ. 243 (2019) 513–521.
[5] P. Chen, H. Wang, H.J. Liu, Z.L. Ni, J.Y. Li, Y. Zhou, F. Dong, Directional electron delivery and enhanced reactants activation enable efficient photocatalytic air purification on amorphous carbon nitride Co-functionalized with O/La, Appl. Catal. B: Environ. 242 (2019) 19–30.
[6] Y. Jiang, F.Q. Qu, L. Tian, X.F. Yang, Z.Y. Zou, Z.X. Lin, Self-assembled $g\text{-}C_3N_4$ nanoarchitectures with boosted photocatalytic solar-to-hydrogen efficiency, Appl. Sur. Sci. 487 (2019) 59–67.
[7] R. Tao, S. Yang, C.L. Shao, X.H. Li, X.W. Li, S. Liu, J. Zhang, Y.C. Liu, Reusable and flexible $g\text{-}C_3N_4/Ag_3PO_4$/Polyacrylonitrile heterojunction nanofibers for photocatalytic dye degradation and oxygen evolution, ACS Appl. Nano Mater. 2 (2019) 3081–3090.
[8] W.N. Xing, W.G. Tu, Z.H. Han, Y.D. Hu, Q.Q. Meng, G. Chen, Template-induced high-crystalline $g\text{-}C_3N_4$ nanosheets for enhanced photocatalytic H_2 evolution, ACS Energy Lett. 3 (2018) 514–519.
[9] T.B. Nguyen, C.P. Huang, R.-A. Doong, Enhanced catalytic reduction of nitrophenols by sodium borohydride over highly recyclable Au@graphitic carbon nitride nanocomposites, Appl. Catal. B: Environ. 240 (2019) 337–347.
[10] G.G. Liu, G.X. Zhao, W. Zhou, Y.Y. Liu, H. Pang, H.B. Zhang, D. Hao, X.G. Meng, P. Li, T. Kako, J.H. Ye, In situ bond modulation of graphitic carbon nitride to construct p-n homojunctions for enhanced photocatalytic hydrogen production, Adv. Funct. Mater. 26 (2016) 6822–6829.
[11] L. Sun, M.J. Yang, J.F. Huang, D.S. Yu, W. Hong, X.D. Chen, Freestanding graphitic carbon nitride photonic crystals for enhanced photocatalysis, Adv. Funct. Mater. 26 (2016) 4943–4950.
[12] D.L. Huang, Z.H. Li, G.G. Zeng, C.Y. Zhou, W.J. Xue, X.M. Gong, X.L. Yan, S. Chen, W.J. Wang, M. Cheng, Megamerger in photocatalytic field: 2D $g\text{-}C_3N_4$ nanosheets serve as support of 0D nanomaterials for improving photocatalytic performance, Appl. Catal. B: Environ. 240 (2019) 153–173.
[13] Q.J. Lu, H.Y. Wang, Y.L. Liu, Y.X. Hou, H.T. Li, Y.Y. Zhang, Graphitic carbon nitride nanodots: As reductant for the synthesis of silver nanoparticles and its biothiols biosensing application, Biosens. Bioelectron. 89 (2017) 411–416.
[14] F. Yang, D.Z. Liu, Y.X. Li, L.J. Cheng, J.H. Ye, Salt-template-assisted construction of honeycomb-like structured $g\text{-}C_3N_4$ with tunable band structure for enhanced photocatalytic H_2 production, Appl. Catal. B: Environ. 240 (2019) 64–71.
[15] A. Mitra, P. Howli, D. Sen, B. Das, K.K. Chattopadhyay, $Cu_2O/g\text{-}C_3N_4$ nanocomposites: an insight into the band structure tuning and catalytic efficiencies, Nanoscale 8 (2016) 19099–19109.
[16] Z. Chen, X. Yu, Q.H. Zhu, T.T. Fan, Q.L. Wu, L.Z. Zhang, J.H. Li, W.P. Fang, X.D. Yi, Steam engraving optimization of graphitic carbon nitride with enhanced photocatalytic hydrogen evolution, Carbon 139 (2018) 189–194.
[17] Y. Huang, P.G. Wang, Z.Y. Wang, Y.F. Rao, J.-J. Cao, S.Y. Pu, W.K. Ho, S.C. Lee, Protonated $g\text{-}C_3N_4/Ti^{3+}$ self-doped TiO_2 nanocomposite films: Room-temperature preparation, hydrophilicity, and application for photocatalytic NO_x removal, Appl. Catal. B: Environ. 240 (2019) 122–131.
[18] Y.J. Zhang, T. Mori, J.H. Ye, M. Antonietti, Phosphorus-doped carbon nitride solid: enhanced electrical conductivity and photocurrent generation, J. Am. Chem. Soc. 132 (2010) 6294–6295.
[19] Z. Zhu, X. Tang, T.S. Wang, W.Q. Fan, Z. Liu, C.X. Li, P.W. Huo, Y.S. Yan, Insight into the effect of Co-doped to the photocatalytic performance and electronic structure of $g\text{-}C_3N_4$ by first principle, Appl. Catal. B: Environ. 241 (2019) 319–328.
[20] W.J. Fang, J.Y. Liu, L. Yu, Z. Jiang, W.F. Shangguan, Novel (Na, O) Co-doped $g\text{-}_C3_N4$ with simultaneously enhanced absorption and narrowed bandgap for highly efficient hydrogen evolution, Appl. Catal. B: Environ. 209 (2017) 631–636.
[21] V.S. Kale, U. Sim, J. Yang, K. Jin, S.I. Chae, W.J. Chang, A.K. Sinha, H.J. Ha, C.-C. Hwang, J. An, H.-K. Hong, Z. Lee, K.T. Nam, T. Hyeon, Sulfur-modified graphitic carbon nitride nanostructures as an efficient electrocatalyst for water oxidation, Small 13 (2017) 1603893.
[22] R. You, H.L. Dou, L. Chen, S.H. Zheng, Y.P. Zhang, Graphitic carbon nitride with S and O codoping for enhanced visible light photocatalytic performance, RSC Adv. 7 (2017) 15842–15850.
[23] Q. Gu, J.N. Liu, Z.W. Gao, C. Xue, Homogenous boron-doping in self-sensitized carbon nitride for enhanced visible-light photocatalytic activity, Chem. Asian J. 11 (2016) 3169–3173.
[24] Q.Y. Guo, Y.H. Zhang, J.R. Qiu, G.P. Dong, Engineering the electronic structure and optical properties of $g\text{-}C_3N_4$ by non-metal ion doping, J. Mater. Chem. C 4 (2016) 6839–6847.
[25] Z. Wei, F.F. Liang, Y.F. Liu, W.J. Luo, J. Wang, W.Q. Yao, Y.F. Zhu, Photoelectrocatalytic degradation of phenol-containing wastewater by $TiO_2/g\text{-}C_3N_4$ hybrid heterostructure thin film, Appl. Catal. B: Environ. 201 (2017) 600–606.
[26] G.H. Dong, L.P. Yang, F. Wang, L. Zang, C.Y. Wang, Removal of nitric oxide through visible light photocatalysis by $g\text{-}C_3N_4$ modified with perylene imides, ACS Catal. 6 (2016) 6511–6519.
[27] Q.L. Tay, X.H. Wang, X. Zhao, J.D. Hong, Q. Zhang, R. Xu, Z. Chen, Enhanced visible light hydrogen production via a multiple heterojunction structure with defect-engineered $g\text{-}C_3N_4$ and two-phase anatase/brookite TiO_2, J. Catal. 342 (2016) 55–62.
[28] R.Q. Ye, H.B. Fang, Y.-Z. Zheng, N. Li, Y. Wang, X. Tao, Fabrication of $CoTiO_3/g\text{-}C_3N_4$ hybrid photocatalysts with enhanced H_2 evolution: Z-Scheme photocatalytic mechanism insight, ACS Appl. Mater. Interf. 8 (2016) 13879–13889.
[29] R.L. Cheng, L.X. Zhang, X.Q. Fan, M. Wang, M.L. Li, J.L. Shi, One-step construction of FeO_x modified $g\text{-}C_3N_4$ for largely enhanced visible-light photocatalytic hydrogen evolution, Carbon 101 (2016) 62–70.
[30] P.X. Qiu, J.H. Yao, H. Chen, F. Jiang, X.C. Xie, Enhanced visible-light photocatalytic decomposition of 2,4-dichlorophenoxyacetic acid over $ZnIn_2S_4/g\text{-}C_3N_4$ photocatalyst, J. Hazard. Mater. 317 (2016) 158–168.
[31] Z.Y. Wang, Y. Huang, W.K. Ho, J.J. Cao, Z.X. Shen, S.C. Lee, Fabrication of $Bi_2O_2CO_3/g\text{-}C_3N_4$ heterojunctions for efficiently photocatalytic NO in air removal: In-situ self-sacrificial synthesis, characterizations and mechanistic study, Appl. Catal. B: Environ. 199 (2016) 123–133.
[32] S.C. Yan, Z.S. Li, Z.G. Zou, Photodegradation of rhodamine B and methyl orange over boron-doped $g\text{-}C_3N_4$ under visible light irradiation, Langmuir 26 (2010) 3894–3901.
[33] N. Sagara, S. Kamimura, T. Tsubota, T. Ohno, Photoelectrochemical CO_2 reduction by a p-type boron-doped $g\text{-}C_3N_4$ electrode under visible light, Appl. Catal. B: Environ. 192 (2016) 193–198.
[34] C.H. Lu, R.Y. Chen, X. Wu, M.F. Fan, Y.H. Liu, Z.G. Le, S.J. Jiang, S.Q. Song, Boron doped $g\text{-}C_3N_4$ with enhanced photocatalytic $U_O^{22}+$ reduction performance, Appl. Sur. Sci. 360 (2016) 1016–1022.
[35] R.R. Hao, G.H. Wang, H. Tang, L.L. Sun, C. Xu, D.Y. Han, Template-free preparation of macro/mesoporous $g\text{-}C_3N_4/TiO_2$ heterojunction photocatalysts with enhanced visible light photocatalytic activity, Appl. Catal. B: Environ. 187 (2016) 47–58.
[36] S.K. Le, T.S. Jiang, Y.W. Li, Q. Zhao, Y.Y. Li, W.B. Fang, M. Gong, Highly efficient visible-light-driven mesoporous graphitic carbon nitride/ZnO nanocomposite photocatalysts, Appl. Catal. B: Environ. 200 (2017) 601–610.
[37] K.C. Christoforidis, T. Montini, E. Bontempi, S. Zafeiratos, J.J.D. Jaèn, P. Fornasiero, Synthesis and photocatalytic application of visible-light active $\beta\text{-}Fe_2O_3/g\text{-}C_3N_4$ hybrid nanocomposites, Appl. Catal. B: Environ. 187 (2016) 171–180.
[38] S.W. Cao, X.-F. Liu, Y.-P. Yuan, Z.Y. Zhang, Y.-S. Liao, J. Fang, S.C.J. Loo, T.C. Sum, C. Xue, Solar-to-fuels conversion over $In_2O_3/g\text{-}C_3N_4$ hybrid photocatalysts, Appl. Catal. B: Environ. 147 (2014) 940–946.
[39] Z.F. Jiang, D.L. Jiang, Z.X. Yan, D. Liu, K. Qian, J.M. Xie, A new visible light active multifunctional ternary composite based on TiO_2–In_2O_3 nanocrystals heterojunction decorated porous graphitic carbon nitride for photocatalytic treatment of hazardous pollutant and H_2 evolution, Appl. Catal. B: Environ. 170–171 (2015) 195–205.
[40] Z.Z. Lin, X.C. Wang, Nanostructure engineering and doping of conjugated carbon nitride semiconductors for hydrogen photosynthesis, Angew. Chem Int. Ed. 52 (2013) 1735–1738.
[41] H.F. Shi, G.Q. Chen, C.L. Zhang, Z.G. Zou, Polymeric $g\text{-}C_3N_4$ coupled with $NaNbO_3$ nanowires toward enhanced photocatalytic reduction of CO_2 into renewable fuel, ACS Catal. 4 (2014) 3637–3643.
[42] H.Q. Li, Y.X. Liu, X. Gao, C. Fu, X.C. Wang, Facile synthesis and enhanced visible-light photocatalysis of graphitic carbon nitride composite semiconductors, ChemSusChem 8 (2015) 1189–1196.
[43] L.Q. Shao, D.L. Jiang, P. Xiao, L.M. Zhu, S.C. Meng, M. Chen, Enhancement of $g\text{-}C_3N_4$ nanosheets photocatalysis by synergistic interaction of ZnS microsphere and RGO inducing multistep charge transfer, Appl. Catal. B: Environ. 198 (2016) 200–210.
[44] S.L. Ma, S.H. Zhan, Y.N. Jia, Q. Shi, Q.X. Zhou, Enhanced disinfection application of Ag-modified $g\text{-}C_3N_4$ composite under visible light, Appl. Catal. B: Environ. 186 (2016) 77–87.
[45] M.Y. Huang, Y.L. Zhao, W. Xiong, S.V. Kershaw, Y.G. Yu, W. Li, T. Dudka, R.Q. Zhang, Collaborative enhancement of photon harvesting and charge carrier dynamics in carbon nitride photoelectrode, Appl. Catal. B: Environ. 237 (2018) 783–790.
[46] L.G. Gai, L. Ma, H.H. Jiang, Y. Ma, Y. Tian, H. Liu, Nitrogen-doped In_2O_3 nanocrystals constituting hierarchical structures with enhanced gas-sensing properties, CrystEngComm 14 (2012) 7479–7486.
[47] X.L. Yang, F.F. Qian, G.J. Zou, M.L. Li, J.R. Lu, Y.M. Li, M.T. Bao, Facile fabrication of acidified $g\text{-}C_3N_4/g\text{-}C_3N_4$ hybrids with enhanced photocatalysis performance under visible light irradiation, Appl. Catal. B: Environ. 193 (2016) 22–35.
[48] A. Li, X.X. Chang, Z.Q. Huang, C.C. Li, Y.J. Wei, L. Zhang, T. Wang, J.L. Gong, Thin heterojunctions and spatially separated cocatalysts to simultaneously reduce bulk and surface recombination in photocatalysts, Angew. Chem. Int. Ed. 55 (2016) 13734–13738.
[49] J.B. Mu, B. Chen, M.Y. Zhang, Z.C. Guo, P. Zhang, Z.Y. Zhang, Y.Y. Sun, C.L. Shao, Y.C. Liu, Enhancement of the visible-light photocatalytic activity of In_2O_3–TiO_2 nanofiber heteroarchitectures, ACS Appl. Mater. Interfaces. 4 (2012) 424–430.

[50] H.F. Shi, C.L. Zhang, C.P. Zhou, G.Q. Chen, Conversion of CO_2 into renewable fuel over Pt-g-C_3N_4/$KNbO_3$ composite photocatalyst, RSC Adv. 5 (2015) 93615–93622.
[51] M. Tasbihi, A. Acharjya, A. Thomas, M. Reli, N. Ambrozova, K. Kocci, R. Schomacker, Photocatalytic CO_2 reduction by mesoporous polymeric carbon nitride photocatalysts, J. Nanosci. Nanotechno. 18 (2018) 5636–5644.
[52] H. Abdullah, M. Maksudur Rahman Khan, H.R. Ong, Z. Yaakob, Modifified TiO_2 photocatalyst for CO_2 photocatalytic reduction: An overview, J. CO_2 Util. 22 (2017) 15–32.
[53] S. Kundu, A. Patra, Nanoscale strategies for light harvesting, Chem. Rev. 117 (2017) 712–757.
[54] J.S. Zhang, G.G. Zhang, X.F. Chen, S. Lin, L. Möhlmann, G. Dołęga, G. Lipner, M. Antonietti, S. Blechert, X.C. Wang, Co-monomer control of carbon nitride semiconductors to optimize hydrogen evolution with visible light, Angew. Chem Int. Ed. 51 (2012) 3183–3187.
[55] W. Chen, T. Huang, Y.-X. Hua, T.-Y. Liu, X.-H. Liu, Hierarchical $CdIn_2S_4$ microspheres wrapped by mesoporous g-C_3N_4 ultrathin nanosheets with enhanced visible light driven photocatalytic reduction activity, J. Hazard. Mater. 320 (2016) 529–538.
[56] Y.B. Jiang, Z.Z. Sun, C. Tang, Y.X. Zhou, L. Zeng, L.M. Huang, Enhancement of photocatalytic hydrogen evolution activity of porous oxygen doped g-C_3N_4 with nitrogen defects induced by changing electron transition, Appl. Catal. B: Environ. 240 (2019) 30–38.
[57] C.Y. Zhai, M.J. Sun, L.X. Zeng, M.Q. Xue, J.G. Pan, Y.K. Du, Construction of Pt/graphitic C_3N_4/MoS_2 heterostructures on photo-enhanced electrocatalytic oxidation of small organic molecules, Appl. Catal. B: Environ. 243 (2019) 283–293.
[58] Z. Zhu, P.W. Huo, Z.Y. Lu, Y.S. Yan, Z. Liu, W.D. Shi, C.X. Li, H.J. Dong, Fabrication of magnetically recoverable photocatalysts using g-C_3N_4 for effective separation of charge carriers through like-Z-scheme mechanism with Fe_3O_4 mediator, Chem. Eng. J. 331 (2018) 615–625.